nature communications

Article

https://doi.org/10.1038/s41467-025-57783-w

Integer topological defects offer a methodology to quantify and classify active cell monolayers

Received: 10 October 2024

Accepted: 27 February 2025

Published online: 12 March 2025

Check for updates

Zihui Zhao[1], He Li[2], Yisong Yao[1], Yongfeng Zhao[3], Francesca Serra[4,5], Kyogo Kawaguchi[6,7,8,9], Hepeng Zhang[1,2] & Masaki Sano[1,2,9]

Monolayers of confluent elongated cells are frequently considered active nematics, featuring $\pm\frac{1}{2}$ topological defects. In extensile systems, where cells extend further along their long axis, they can accumulate at $+\frac{1}{2}$ defects and escape from $-\frac{1}{2}$ defects. Nevertheless, collective dynamics surrounding integer defects remain insufficiently understood. We induce diverse +1 topological defects (asters, spirals, and targets) within neural progenitor cell monolayers using microfabricated patterns. Remarkably, cells migrate toward the cores of all +1 defects, challenging existing theories and conventional extensile/contractile dichotomy, which predicts escape from highly bent spirals and targets. By combining experiments and a continuum theory derived from a cell-level model, we identify previously overlooked nonlinear active forces driving this unexpected accumulation toward defect cores, providing a unified framework to explain cell behavior across defect types. Our findings establish +1 defects as probes to uncover key nonlinear features of active nematics, offering a methodology to characterize and classify cell monolayers.

Elongated cells forming confluent monolayers have been described as nematic liquid crystals—passive[1] or, more recently, active[2–5]. Similar to the passive case, active nematics exhibit half-integer topological defects[6–14]. Recently gathered evidence shows that $+\frac{1}{2}$ defects can be the location of cell accumulation or cell extrusion[15,16]. Particularly, this is observed in the confluent monolayers of neural progenitor cells (NPCs) and epithelials[16]. Hydrodynamic theories based on the classical description of extensile linear active forces qualitatively explain these findings[11,15,16]. However, confusion arising from observations that isolated cells are contractile has resulted in the development of a theory based on fluctuations in cellular velocity[17,18].

Integer topological defects are also prevalent in nature and biologically relevant, such as asters in a neural rosette, targets in plants meristem; and asters and targets during the morphogenesis of hydra[19–23] (target is also called vortex in liquid crystal terminology). Integer defects do not occur spontaneously in nematics as they tend to split into pairs of half-integer defects. However, such defects can be induced via external factors and thus play crucial biological functions. Recently, in vitro studies demonstrated that +1 defects induced by circular confinement serve as sites of attraction and cellular differentiation in C2C12 myoblasts[24], +1 defects induced by target patterns in fibroblast monolayers increase cell density at defect cores[25,26]. The former case was theoretically attributed to extensile active stress[27],

[1]School of Physics and Astronomy, Shanghai Jiao Tong University, Shanghai, China. [2]Institute of Natural Sciences, Shanghai Jiao Tong University, Shanghai, China. [3]Center for Soft Condensed Matter Physics and Interdisciplinary Research, Soochow University, Suzhou, China. [4]Physics and Astronomy, Johns Hopkins University, BA, USA. [5]Department of Physics, Chemistry and Pharmacy, University of Southern Denmark, Odense, Denmark. [6]Institute for Physics of Intelligence, The University of Tokyo, Tokyo, Japan. [7]Nonequilibrium Physics of Living Matter RIKEN Hakubi Research Team, RIKEN Center for Biosystems Dynamics Research, Kobe, Japan. [8]RIKEN Cluster for Pioneering Research, Kobe, Japan. [9]Universal Biology Institute, The University of Tokyo, Tokyo, Japan. e-mail: sano.masaki@sjtu.edu.cn

although the C2C12 monolayers had previously been considered contractile[15]. They also considered nematic contribution in the active forces but concluded that it did not introduce new effects in spirals and asters. This indicates that the classification of active cell monolayers via the extensile/contractile dichotomy may be inadequate. In the latter case, a high cell division rate at defect cores was inferred[26], instead of the large-scale motion of cells typically predicted by hydrodynamic theories. Despite biological importance, comprehensive quantitative measurements of tissue properties and large-scale hydrodynamics in stable, well-defined defects are still lacking.

At high density, NPCs assume elongated shapes and exhibit a stochastic back-and-forth motion without apparent contact inhibition or strong cell–cell adhesion[15], showing a nematic order. These characteristics make NPCs an excellent system for developing the hierarchical descriptions of active nematics, from an individual cell level to a continuum theory.

To investigate the behavior of cellular active nematics with integer defects, we induce +1 defects in NPC monolayers via cell culturing on patterned substrates. We consider a one-parameter family of +1 defects, ranging from asters to targets via spirals. In all cases, cells accumulate at the defect cores and exhibit large-scale inward flows toward defect cores. Furthermore, we show that our findings cannot be explained by the linear active force model with the extensile/contractile dichotomy, which is used in hydrodynamic theories for the unpatterned case, as this model predicts outward flows for strongly bent spirals and targets. Hence, we derive a nonlinear hydrodynamic theory using a minimal particle-/cell-level model that incorporates the essential features of the system. This theory is summarized in this article and detailed elsewhere[28]. The experimental results reveal that nonlinear active force terms, neglected in conventional approaches, play a crucial part in explaining cellular flows. We estimate all the coefficients that characterize the theory. Our general results indicate a new classification of active nematics and reveal important forces that were previously overlooked.

Results

NPCs accumulate at the cores of +1 topological defects

To investigate the effect of +1 topological defects on cell monolayers, we cultured NPCs on microfabricated polydimethylsiloxane (PDMS) patterns featuring various defect types delineated by 1.2-μm-high ridges (Fig. 1a, Methods). The local orientation θ_p of the ridge pattern was designed via the definition of +1 defects: $\theta_p = \phi + \theta_0$, where ϕ is the polar angle, θ_0 ($\theta_0 \in (-\pi/2, \pi/2]$) is the tilt angle relative to the radial direction (Fig. 1b)[29]. Although each ridge was spaced from its neighbors, hereafter, we used θ_p to denote the reference angle inducing defects and θ to denote the experimentally measured cell orientation, both defined throughout the space around each defect. Specific θ_0 values used were as follows: $\theta_0 = 0, \pm\pi/12, \pm\pi/6, \pm\pi/4, \pm\pi/3, \pm 5\pi/12$, and $\pi/2$. Notably, $\theta_0 = 0$, $0 < \theta_0 < \pi/2$, $-\pi/2 < \theta_0 < 0$, and $\theta_0 = \pi/2$, corresponded to asters, counterclockwise spirals, clockwise spirals, and targets, respectively

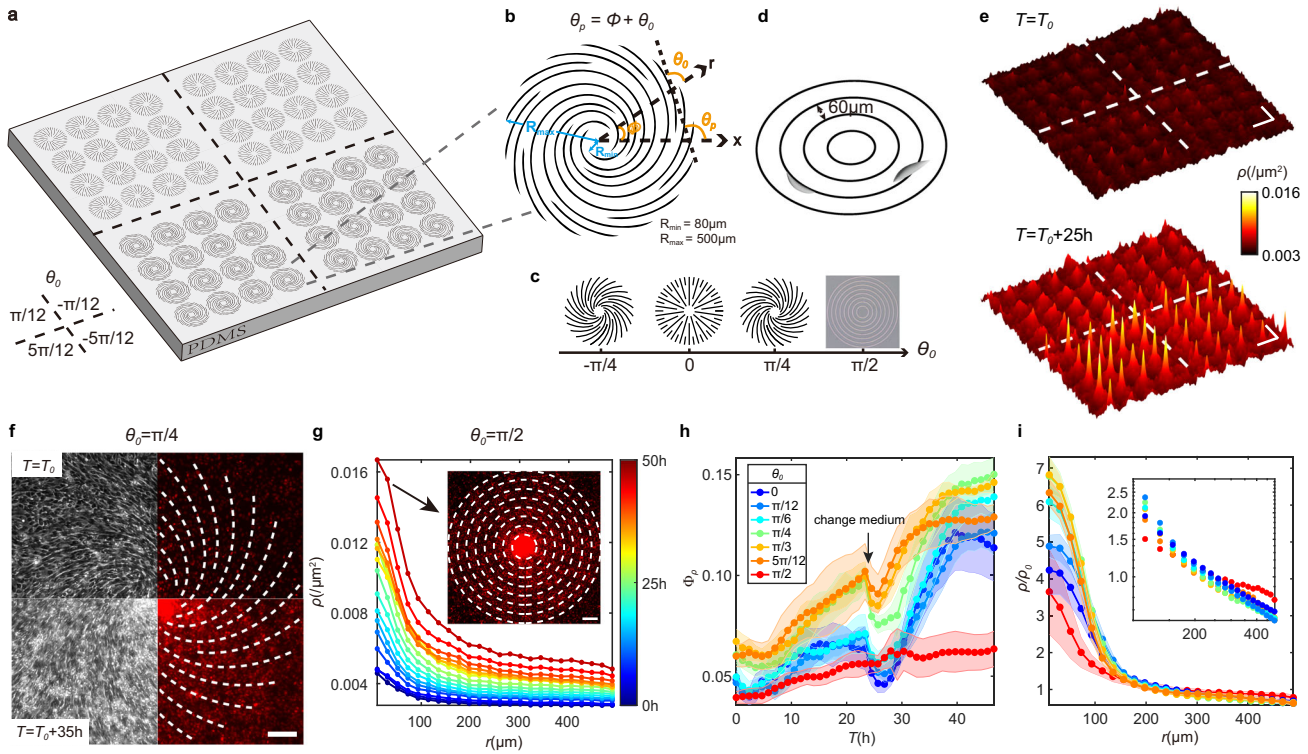

Fig. 1 | Neural progenitor cells (NPCs) accumulate at the centers of asters, spirals, and targets. a Schematic of microfabricated patterns on a polydimethylsiloxane (PDMS) substrate. Four arrays of various spirals ($\theta_0 = \pm\pi/12$ and $\pm 5\pi/12$) are arranged on a PDMS sheet, featuring 16 micropatterns per defect type. **b** Micropatterns designed based on the definition of +1 topological defects. The largest radius of patterns, R_{max}, is 500 μm. The radius of the defect core without ridges, R_{min}, is 80 μm. The distance between ridges is 30–120 μm. **c** Types of +1 topological defects characterized by the tilt angle θ_0. A bright-field image is shown for a target. **d** Cell motion on a target pattern. **e** Heatmap of cell densities on spirals shown in **a** at the beginning and after 25 h of recording. $T = T_0$ at the onset of confluence. **f** Typical phase-contrast images and typical fluorescence images at the beginning and after 35 h of recording on a spiral with $\theta_0 = \pi/4$. Dashed lines depict ridges of patterns. **g** Time evolution of average radial density profiles on the target. Data are averaged every 1 h across 32 targets. Inset: a typical fluorescence image showing cell accumulation after 50 h of recording on a target. Dashed lines depict ridges. **h** Average percentage of cells Φ_ρ ($\Phi_\rho = n(r < R_{min})/n(r < R_{max})$, where n represents cell number) assembling with time on asters, counterclockwise spirals, and targets. Different colors depict various defect types. The number (N) of each defect type is six, and all defects are designed on the single PDMS sheet. **i**, Radial density profiles normalized by mean density ρ_0 when $\rho_0 = 0.009$ /μm^2. Inset: A log--log plot for the region with $r > 100$ μm. N values for aster, each type of spiral, and target are 32, 6, and 32, respectively. Legend in **h**. In **h** and **i**, data are presented as mean ± standard deviation (s.d.), and s.d. values are calculated from defects in an array. Scale bars: 100 μm.

(Fig. 1c). The patterns had a maximal radius R_{max} = 500 μm and included a central, ridge-less area with a radius R_{min} of 80 μm. The shallow ridges were considered to constitute weak external fields because the cells easily climbed and crossed over them (Fig. 1d, Supplementary Video 1). They gently guided the cells and induced +1 defects in the confluent cell monolayers (Fig. 1f).

We conducted long time-lapse recordings after confluence and observed that cells gradually accumulated with time at the cores of defects irrespective of θ_0 (Fig. 1e, f, g, Methods). The local cell density ρ was measured via nuclear fluorescence intensity (Methods). Upon azimuthally averaging the configurations, we obtained the time evolution of cell density's radial profiles across all patterns (Fig. 1g, Supplementary Fig. 1a and 2a). The ratio Φ_ρ, representing the number of cells within radius R_{min} around defect cores relative to total number of cells, exhibited a continuous increase except during periods of medium changes (Fig. 1h, Supplementary Fig. 1b and 2b, Supplementary Video 2). Radius-dependent average cell densities on various defects with same total density exhibited distinct accumulations around cores and similar slopes in the log–log plot in regions outside cores (Fig. 1i, Supplementary Fig. 1c). In addition, the accumulation behaviors were more prominent on the counterclockwise patterns, potentially attributable to the weak chirality of NPCs (Supplementary Fig. 2b and c)[30].

Three-dimensional (3D) mounds formed at defect cores when cell density was high, while regions outside the centers remained predominantly two-dimensional (2D). Analyzing the basal plane using confocal microscopy (Methods, Supplementary Information: Section 9), we found that time evolution of radial density profiles showed higher density around the defect cores (Supplementary Fig. 14d). However, as the center density became too high, cells migrated into the third dimension, forming 3D mounds, which led to a relatively stable central density on the basal plane. Meanwhile, cell division continued outside the centers, where the lower density allowed for a sustained increase in the 2D density. Therefore, we observed that Φ_ρ in the basal plane decreases relatively over time, but the density at the core remained higher than the outer region all the time (Supplementary Fig. 14e).

Orientations and dynamics of NPCs in induced topological defects

When forming a confluent monolayer, cells tended to align their elongated shapes with their neighbors and guiding patterns (Fig. 2a–c). The local orientation of this nematic order barely changed throughout the recording. We obtained local nematic orientational fields by applying structure tensor method to phase-contrast images and locally averaged orientations over space and time (Fig. 2a–c, Supplementary Fig. 3a, Methods). We calculated the local scalar order parameter S to quantify the degree of the orientational order. S values were minimal at the cores, increased with defect radius, and slightly decreased near the edges due to weaker guidance from wider ridge spacing (Fig. 2d, Supplementary Fig. 3d). Orientation measurements

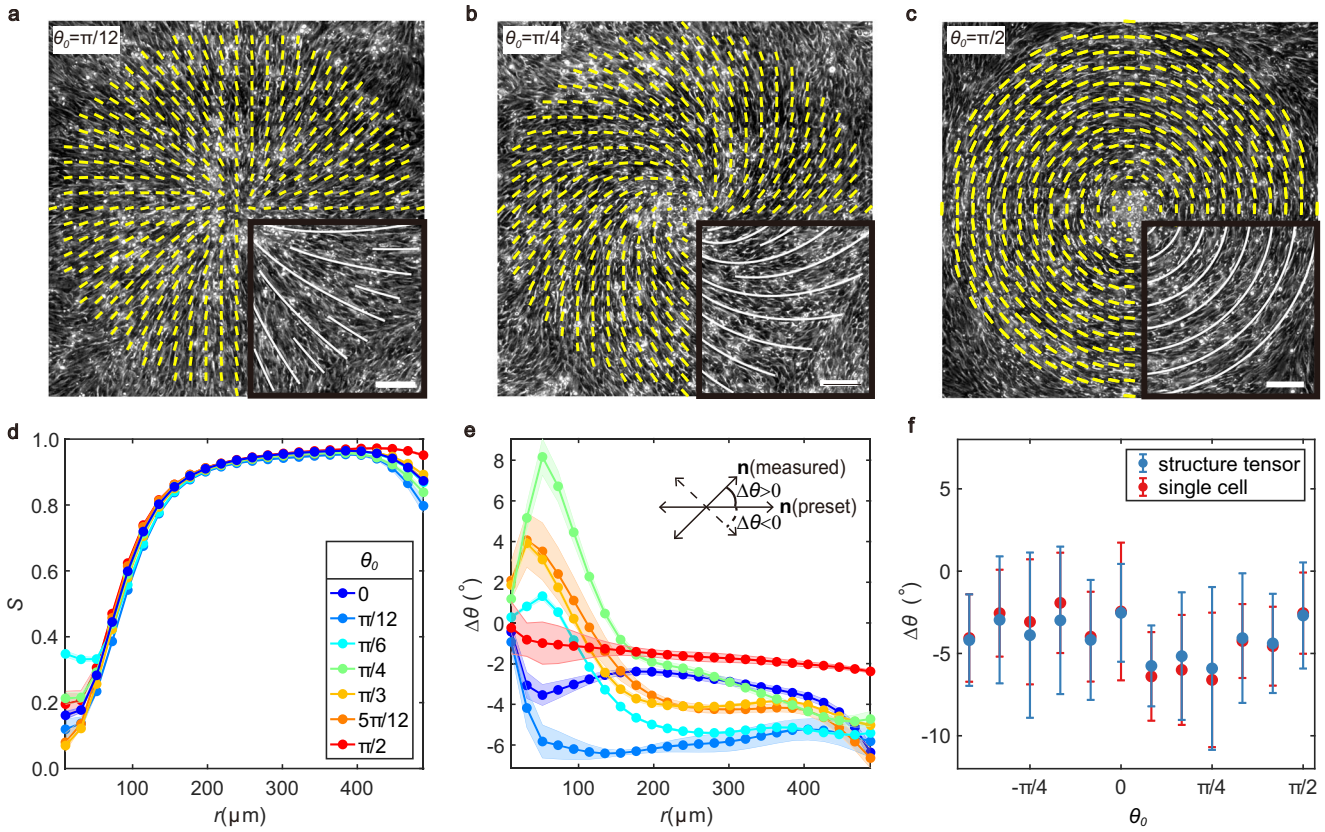

Fig. 2 | Cellular orientations around induced +1 defects. a–c Spatiotemporally averaged orientational fields on defect patterns with $\theta_0 = \pi/12$, $\pi/4$, and $\pi/2$, respectively. Yellow lines depict local nematic orientations, with their lengths corresponding to local coherency. Background: phase-contrast images, from which cell bodies can be observed. Insets: white lines show shallow ridges of patterns. **d** Radial profiles of the order parameter S on asters, counterclockwise spirals, and targets. **e** Radial profiles of the angles $\Delta\theta$ between the experimentally measured cell orientations and orientations preset by the PDMS patterns on asters, counterclockwise spirals, and targets. Preset orientation refers to a cellular alignment in which cells form perfect topological defects. Inset shows the definition of $\Delta\theta$: $\Delta\theta > 0$ when the measured orientation (measured $\mathbf{n} = (\cos\theta, \sin\theta)$) rotates counterclockwise against the preset orientation (preset $\mathbf{n} = (\cos\theta_p, \sin\theta_p)$), and $\Delta\theta < 0$ for clockwise rotation. **f** $\Delta\theta$ across all defect types. In **a**–**f**, data are averaged across 32 asters (10 h), 16 spirals of each type (10 h), and 32 targets (10 h). In **d**, **e**, data are presented as mean ± s.d., and s.d. are calculated at various times during 10 h. In **f**, data are presented as mean ± s.d., and s.d. are calculated using various positions of average orientational fields (regions with $r < 100$ μm are excluded). Scale bars: 100 μm.

around defect cores were less accurate due to the high densities at the cores. Coherency analysis showed that orientation estimates outside defect cores were more reliable (Supplementary Fig. 3e and f, Methods).

To evaluate how effectively guiding ridges induced +1 defects, we measured the angle $\Delta\theta$ between the local cell orientation (θ) and the preset defect orientation (θ_p). We observed that the values of $\Delta\theta$ did not considerably change with the radius (Fig. 2e, Supplementary Fig. 3g). We averaged $\Delta\theta$ in regions with $r > 100\,\mu$m and consistently observed that they were approximately $-4.1 \pm 1.1^{\circ}$ for all defects (standard deviations (SDs) as errors), indicating a weak clockwise chirality (Fig. 2f). Comparable results were obtained via orientational fields derived from the long axis of nuclei (Fig. 2f, Supplementary Fig. 3b and c, Methods). These small values of $\Delta\theta$ confirmed the successful induction of designed defects into cell monolayers.

We conducted a quantitative analysis of cell dynamics to investigate whether the aggregation around defect cores was associated with collective movements. Trajectories depicted in (Fig. 3a–b) were extracted by tracking cell nuclei (Methods, Supplementary Videos 3–6). Individual cells exhibited bidirectional motion with an instantaneous speed of approximately $0.44 \pm 0.02\,\mu$m/ min (SDs as errors) and a typical reversal time of 1–2 h (Fig. 3c, Methods). By coarse-graining instantaneous velocities during the continuous accumulation periods (10 h, as shown in Fig. 1h), we obtained spatio-temporally averaged net velocity fields (Supplementary Fig. 4a, Methods, see Supplementary Videos 3–6 for time evolution of spatially averaged net velocity fields). Streamlines calculated using these net velocity fields demonstrated the inward direction of cellular flows (Fig. 3d–f). Notably, one can see that the local net velocities were typically not aligned with the local orientations. Averaging radial net velocities along the azimuthal direction showed inward net radial velocities for all defects (Fig. 3g, Supplementary Fig. 4b). In our measurements here and subsequent fitting process, we considered a timescale of 10 h, during which cells did not considerably proliferate because cell division typically takes approximately 24 h[15].

We further analyzed the probability distribution functions of angles (θ_v) between net velocities and inward radial directions. We excluded regions corresponding to $r < 100\,\mu$m to avoid inaccuracies associated with tracking single cells in high-density cores. These angles (θ_v) were predominantly situated in the inward region ($-90^{\circ} < \theta_v < 90^{\circ}$) (Fig. 3h). After extracting the peak location of θ_v for each defect in (Fig. 3h) and defining measured tilt angle (θ_0(measured) $\equiv \theta_0 + \Delta\theta$), we finally deduced the manner by which θ_v changed with the θ_0(measured) (Fig. 3i). The obtained results were comparable with those from the optical flow method (Supplementary Fig. 4c and d, Methods). Symmetry-breaking shown in Fig. 2f, Fig. 3f, h indicates chirality.

Detecting the relation between net cellular flows and active forces

Typically, conventional active nematic theories include an equation relating a net velocity field with a linear active force term:

$$\gamma \mathbf{v} = -\zeta \nabla \cdot \mathbf{Q} \tag{1}$$

where γ represents friction coefficient between cell monolayers and substrate, and $\mathbf{Q} = S\begin{pmatrix} \cos(2\theta) & \sin(2\theta) \\ \sin(2\theta) & -\cos(2\theta) \end{pmatrix}$ represents the nematic tensor order parameter, with θ representing local cell orientation. The linear active force ($\mathbf{f}$) can be formally identified as divergence of active stress $-\zeta\mathbf{Q}$, resulting in $\mathbf{f} = -\zeta \nabla \cdot \mathbf{Q}$[31,32]. In the unpatterned case, $+\frac{1}{2}$ defects in the confluent NPCs were observed to move in the direction of the comet head[15,33], a characteristic of an extensile system with $\zeta > 0$.

In our experiments, cells aligned well with the guiding patterns, leading to a considerably slower timescale for $\mathbf{Q}$ dynamics than for accumulation processes. Therefore, we assumed $\mathbf{Q}$ was fixed in time by the external field induced by the pattern. For +1 defects with $\theta = \theta_p = \phi + \theta_0$, the linear active force field becomes $\mathbf{f} = -\zeta[S'(r) + \frac{2S(r)}{r}](\cos 2\theta_0 \hat{\mathbf{r}} + \sin 2\theta_0 \hat{\boldsymbol{\phi}})$, where $S'(r) = \frac{dS(r)}{dr}$, and $\hat{\mathbf{r}}$ ($\hat{\boldsymbol{\phi}}$) represents unit vector in the radial (azimuthal) direction. In a uniform and confluent state where $S'(r) > 0$ near the cores, the radial component is inward for $0 \le |\theta_0| < \pi/4$ but outward for $\pi/4 < |\theta_0| \le \pi/2$, predicting outward flows for large values of $|\theta_0|$ (Fig. 4a). This is in conflict with the inward flows observed for all types of induced +1 defects.

The linear theory can be refined by considering the anisotropic friction $\gamma = \gamma_0(I - \epsilon\mathbf{Q})$, with the anisotropy coefficient $0 \le \epsilon \le 1$ representing larger friction along the direction perpendicular to cell alignment[11,15]. However, a comparison of the measured θ_v with θ_v predicted from this extended simple theory showed that the theory failed to explain the inward cellular flows for all defect types (Fig. 3i).

We modeled our system to understand the underlying mechanisms driving inward cellular flows, starting from a minimal particle-/cell-level dry active nematic model where induced patterns were attributed to some external field (Supplementary Information)[28]. Numerical simulation results of this model showed particle accumulation irrespective of types of +1 defects, broadly agreeing with our experimental results. Confident in this model, we derived from it a nonlinear hydrodynamic theory using a Boltzmann–Ginzburg–Landau approach (Supplementary Information: Section 6)[28,34–36]. The theory showed the presence of two nonlinear active force terms in addition to the standard active force. Incorporating these terms and accounting for spatial density variations, the total active force replacing $\mathbf{f}$ was expressed as

$$\mathbf{f}^a = -\zeta \nabla \cdot \rho\mathbf{Q} + \gamma_2 \rho\mathbf{Q} \cdot (\nabla \cdot \rho\mathbf{Q}) + \gamma_1 (\rho\mathbf{Q} \cdot \nabla) \cdot \rho\mathbf{Q}. \tag{2}$$

In the steady state with ideal orientations, $\theta = \theta_p = \phi + \theta_0$, eq. (2) can be written in polar coordinates as

$$f_r^a = \left[(\rho S(r))' + 2\frac{\rho S(r)}{r}\right](-\zeta \cos 2\theta_0 + \gamma_2 \rho S(r)) + \left[(\rho S(r))' - 2\frac{\rho S(r)}{r}\right]\gamma_1 \rho S(r). \tag{3}$$

$$f_\phi^a = -\left[(\rho S(r))' + 2\frac{\rho S(r)}{r}\right]\zeta \sin 2\theta_0, \tag{4}$$

where $(\rho S(r))' = \frac{d(\rho(r)S(r))}{dr}$. Our derivation showed that $\gamma_2 < 0$ and that $\gamma_1 > 0$ generally holds in most cases (Supplementary Information: Section 6). Therefore, the two nonlinear active forces pointed toward the defect cores, which contributed to inward flows and central cell accumulations (Fig. 4a) (Notably, a $\mathbf{Q} \cdot (\nabla \cdot \mathbf{Q})$ term was considered in[37] in the context of active suspensions, where it was shown to stabilize the nematic order). Because our continuum theory included a flow term proportional to the density gradient, the net velocity of cellular flow was governed by

$$\Gamma \rho \mathbf{v} = \mathbf{f}^a - \pi_0 \nabla \rho, \tag{5}$$

where $\Gamma = \gamma_0(I - \epsilon\rho\mathbf{Q})$, $0 \le \epsilon\rho \le 1$ and $\pi_0 > 0$.

To test the relation between cellular flows and active forces from experimental data, we decomposed each of them into parallel and perpendicular components relative to the principal axis of local $\mathbf{Q}$ in regions outside defect cores (Supplementary Fig. 5). In Fig. 4b–d, we have shown parallel components on asters and spirals ($\theta_0 = \pi/4$) and perpendicular components on targets and spirals ($\theta_0 = \pi/4$), as they represent the primary components associated with inward flows on the corresponding patterns. Concerning the $\nabla \cdot \rho\mathbf{Q}$ term, the parallel components exhibited negative correlations with net velocity, while the perpendicular components showed positive correlations (Fig. 4b), another indication that the linear theory cannot completely explain the observed phenomena. However, these components showed a

https://doi.org/10.1038/s41467-025-57783-w

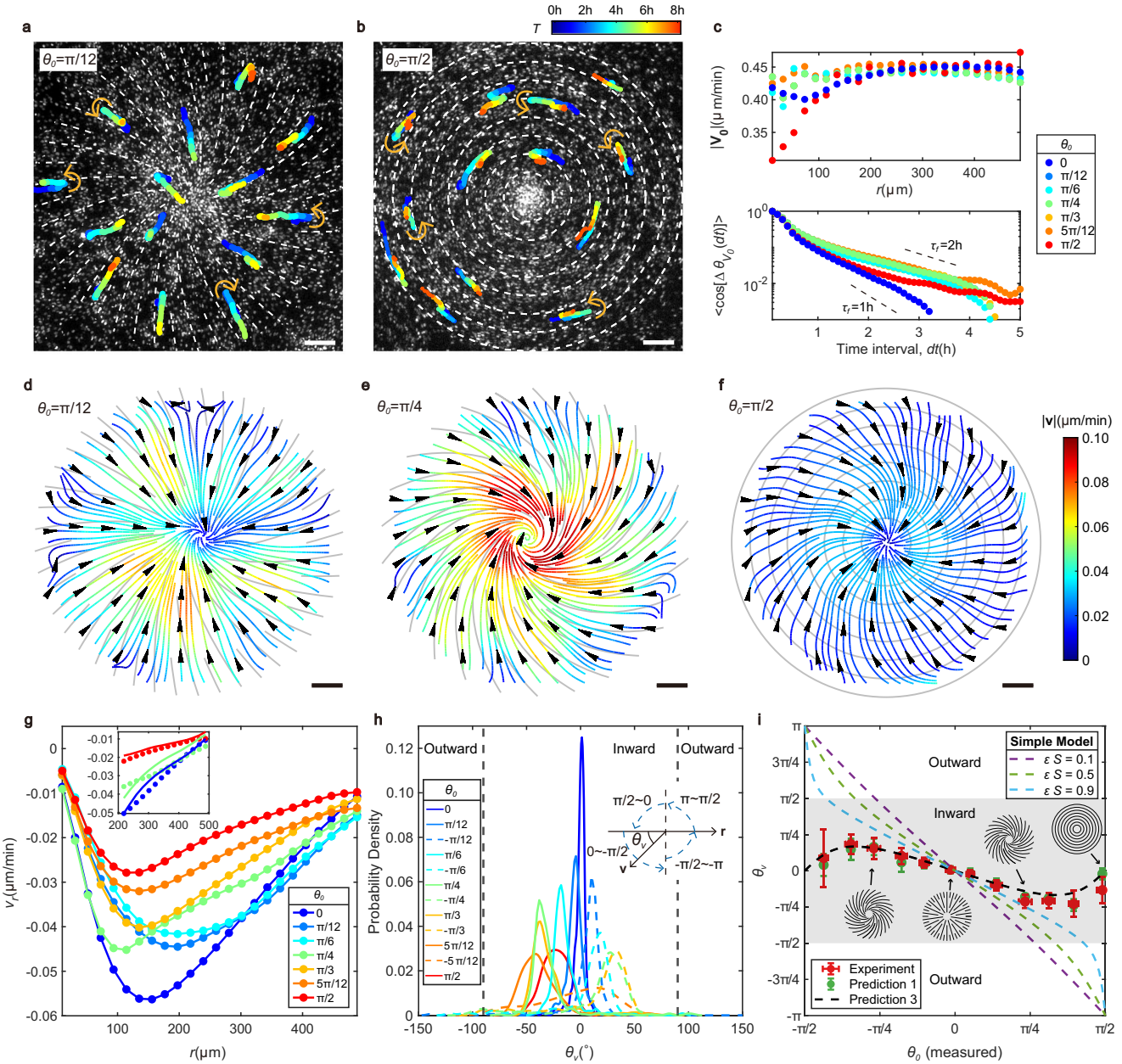

Fig. 3 | Cellular dynamics during accumulation toward +1 defect cores. **a**, **b**, Bidirectional motion of individual NPCs on defects with $\theta_0 = \pi/12$ and $\pi/2$, respectively. Trajectories traveled in time are indicated by color. Color bar in (**b**). Background: fluorescence images, from which cell nuclei can be observed. Dashed lines indicate the guiding ridges of patterns. **c** Radial profiles of the amplitudes of instantaneous velocities (V_0) when mean densities are approximately 0.005 /μm^2 (upper) and autocorrelations of the directions (θ_{V_0}) of the instantaneous velocities as functions of time interval dt (lower). τ_f = 2 h (τ_f = 1 h) corresponds to a reversal time of 2 h (1 h). **d**–**f** Streamlines on defects with $\theta_0 = \pi/12$, $\pi/4$, and $\pi/2$. Gray lines indicate guiding ridges. Color represents the amplitude of net velocities. Color bar in **f**. **g** Radial profiles of the average radial net velocity (V_r) components on asters, counterclockwise spirals, and targets. Inset: Comparison between experimentally measured radial velocities (dots) and predictions (lines) for large r values on asters, spirals ($\theta_0 = \pi/4$), and targets. The prediction is obtained using method (ii). **h** Probability density functions (PDFs) of the angles (θ_v) between net velocities and inward radial directions for all defect types. Insets show the definition of θ_v. **i**, Measured and predicted θ_v values versus measured θ_0 values. θ_0(measured) = $\theta_0 + \Delta\theta$. Prediction 1 (3) is obtained using method (i) ((iii)). Data are presented as mean ± s.d. in the horizontal axis, and the location of peak ± full width at half maximum (FWHM) of PDF shown in **h** in the vertical axis. FWHM and s.d. are calculated using various positions of average net velocity fields (regions with $r < 100\,\mu$m are excluded). In **c**–**i**, data are averaged across 32 asters (10 h), 16 spirals of each type (10 h), and 32 targets (10 h). Scale bars: 100 μm.

consistent negative correlation (Fig. 4c) for the $\rho\mathbf{Q}\cdot(\nabla\cdot\rho\mathbf{Q})$ term and a consistent positive correlation (Fig. 4d) for the $(\rho\mathbf{Q}\cdot\nabla)\cdot\rho\mathbf{Q}$ term. These results provided evidence for the relevance of the two nonlinear active forces to cellular flows.

Predicting cellular flows from local orientations

From the experimental data, we extracted the value of each term in Eq. (2), (5) using the average net velocities, orientations, and densities. To quantitatively assess our theory, we identified the best-fit values of the coefficients in Eq. (2), (5) via the Bayesian inference method (Methods) applied to outer regions ($100\,\mu\text{m} < r < 500\,\mu\text{m}$). During fitting, we replaced ρ in Eq. (2), (5) with the normalized density ρ/ρ_0, where ρ_0 represents mean density. The fits yielded values for five model parameters: $\epsilon' = \rho_0\epsilon, \zeta' = \zeta/\gamma_0, \gamma_2' = \gamma_2\rho_0/\gamma_0, \gamma_1' = \gamma_1\rho_0/\gamma_0$, and $\pi_0' = \pi_0/\gamma_0$. For each defect type, we determined the best-fit values (Supplementary Tab. 1) and then averaged these values across various defect

https://doi.org/10.1038/s41467-025-57783-w

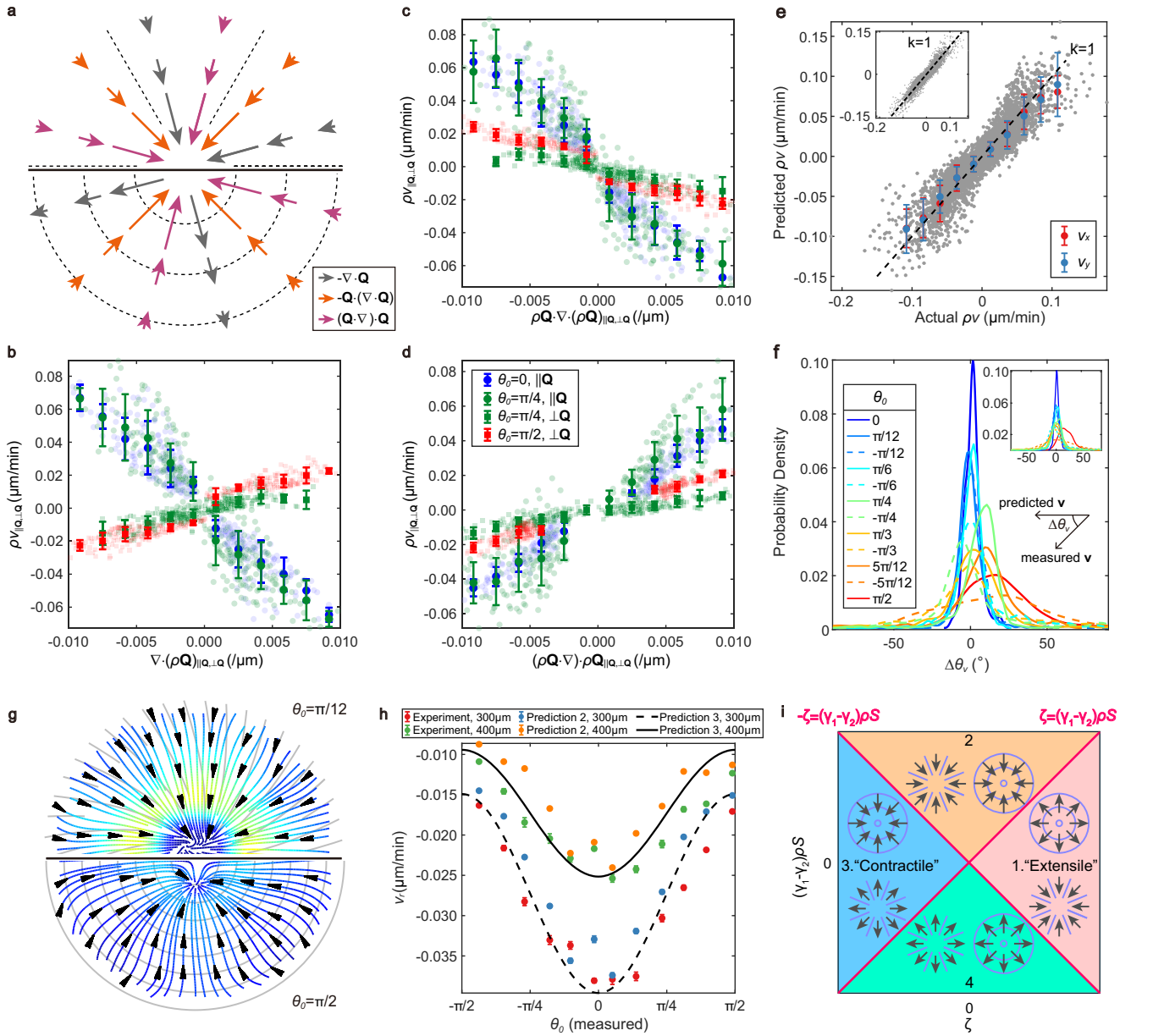

Fig. 4 | Prediction of cellular flows using active forces. a Active forces on asters and targets when S is constant. A long arrow indicates the correspondingly strong force. Comparisons between components of cellular flow ρv and those of active forces $\nabla\cdot(\rho\mathbf{Q})$ (**b**), $\rho\mathbf{Q}\cdot(\nabla\cdot\rho\mathbf{Q})$ (**c**), and $(\rho\mathbf{Q}\cdot\nabla)\cdot\rho\mathbf{Q}$ (**d**). $\rho v_{\parallel\mathbf{Q}}(\rho v_{\perp\mathbf{Q}})$ is defined as the flow component parallel (perpendicular) to the principal axis of Q, similar to the components of active forces. Comparisons between parallel components are plotted for asters and spirals ($\theta_0 = \pi/4$); Comparisons between perpendicular components are plotted for targets and spirals ($\theta_0 = \pi/4$). Error bars represent s.d. **e** Comparison between experimentally measured and predicted cellular flows. The determined coefficient $R^2 = 0.8173$. The scatter plot denotes raw data (grey) on all patterns (regions with $r < 100\,\mu$m are excluded). Symbols show the average values of predictions. The prediction method used is method (ii). Error bars represent s.d. Insets show the results of the prediction method (**i**). In (**b**–**e**), ρ is normalized by mean density. **f** Probability density functions of the angles ($\Delta\theta_v$) between experimentally measured and predicted net velocities. The prediction method used is method (ii). Insets show the definition of $\Delta\theta_v$ and results obtained from prediction method (**i**). **g** Predicted streamlines on the spiral ($\theta_0 = \pi/12$) and target. Color bar in Fig. 3f. The prediction method used is method (**i**). **h** Comparison between measured and predicted net radial velocities at $r = 300$ and $r = 400\,\mu$m for all defects. The method used for prediction 2 (3) is method (ii), (iii). Data are presented as mean ± standard error of the mean (s.e.m.). i New classification of active nematics. Functions defining two red lines are shown on the top left and top right.

types to yield $\epsilon' = 0.148 \pm 0.088$, $\zeta' = 0.0289 \pm 0.0131\,\mu\text{m}^2/\text{s}$, $\gamma_2' = -0.0257 \pm 0.0153\,\mu\text{m}^2/\text{s}$, $\gamma_1' = 0.0564 \pm 0.0144\,\mu\text{m}^2/\text{s}$, and $\pi_0' = 0.0732 \pm 0.0294\,\mu\text{m}^2/\text{s}$, with SDs as errors. Although the SD in these coefficients were large due to differences in cell conditions, the signs of these coefficients—$\zeta'>0$, $\gamma_2'<0$, and $\gamma_1'>0$—were maintained.

We implemented three distinct approaches to predict cellular flows based on eq. (5). (i) We used the experimentally measured $\mathbf{Q}$ and ρ fields for each defect type with best-fit parameters; (ii) employed the same fields but used average parameters; and (iii) generated an $S(r)$ profile and a $\rho(r)$ profile via averaging order parameters and densities respectively across all defects, and used average parameters and active force components in Eq. (3), (4). By comparing the amplitudes and angles of measured and predicted net velocities, we discovered that although the best-fit parameters in method (i) yielded the most accurate predictions, the average parameters in method (ii) provided acceptable predictions (Fig. 4e, f). Using methods (i) and (ii), we predicted velocity fields for all defects (Supplementary Fig. 6a and 7a) and displayed streamlines on a spiral and target (Fig. 4g). In Supplementary Fig. 8 and Fig. 3g, we compared the predicted and measured net radial and azimuthal velocity profiles. Furthermore, in regions outside centers, where

the $\rho(r)$ profiles and the $S(r)$ profiles of all defect types are similar (Fig. 1i, Fig. 2d, Supplementary Fig. 1c and 3d), the measured and predicted net radial velocities exhibited the same cosine-like tendency over θ_0 (Fig. 4h), consistent with the radial components of active forces in eq. (3). Moreover, the predicted tendency of θ_v over θ_0 almost matched the measured tendency, sharply contrasting with the simple theory (Fig. 3i, Supplementary Fig. 4d, S6b and S7b). In the prediction, we obtained slight outward flows at cores of defects with large $|\theta_0|$ (Fig. 4g, Supplementary Fig. 8a and b). Using ideal orientations and setting $\pi'_0 = 0$ at central regions via an assumption, the outward cellular flows essentially vanished (Supplementary Fig. 9, Methods).

We finally propose a classification of dry, active nematics on the basis of our observed phenomena, given that our system cannot be simply categorized as contractile or extensile (as determined by the sign of ζ) owing to the nonlinear active forces. Ignoring the gradients of ρ and S in eq. (3), the direction of force along the radial direction is governed by the relative magnitudes of $\pm\zeta$ and $(\gamma_1 - \gamma_2)\rho S$, where $+(-)$ is for target (aster). Two new cases (regions 2 and 4 in Fig. 4i) emerge when the nonlinear active forces dominate the linear terms ($(\gamma_1 - \gamma_2)\rho S > \pm\zeta$), in which the centers of target and aster could be simultaneously attractive or repulsive. In our case, NPC monolayers are situated in region 2.

Discussion

In nematic monolayers, a paradox arises: $+\frac{1}{2}$ defect moves toward the head of the comet-like structure, suggesting extensile behavior, while traction stress increases toward the tail, resembling contractile behavior[10]. Balasubramaniam et al.[10] studied the extensile-contractile transition in MDCK cells by knocking out E-cadherin, which weakened cell-cell adhesions. This change caused $+\frac{1}{2}$ defect motion to shift from headward to tailward. Their phase field model, incorporating linear active force, reproduced experiments by eliminating intercellular linear active force. However, why weaker contraction resulted in more contractile behavior ($+\frac{1}{2}$ defect moves to tail) remained unsolved. In contrast, our model does not include cell-cell adhesions, consistent with NPCs' properties, and nonlinear active forces do not affect the accumulation/depletion around $\pm 1/2$ defects. These nonlinear terms isotropically direct inward toward $+\frac{1}{2}$ defect cores and outward from $-\frac{1}{2}$ defect cores. The major difference appears in the integer defects. Typically, for target and tightly bend spirals, models only with linear active force predict cell depletion from (attraction to) cores in extensile (contractile) cases. Phase field model in ref. 10 relied on linear forces, making it difficult to capture our $+1$ defect results. On the other hand, our continuum model does not resolve the paradox on traction force. Further research is needed in the future.

Recently, Nejad et al.[38] reported that the angle between shape and stress orientation was widely distributed in MDCK monolayers but more restricted in LP-9 monolayers, likely due to chaotic collective motion in MDCK cells. They also found that MDCK cells had a low aspect ratio (~1.2), leading to large fluctuations in director measurements and weak nematic order. This may prompt a reconsideration of the extensile/contractile dichotomy. In our case, NPCs exhibit a high aspect ratio (5–8), resulting in stronger nematic order. Their continuum model treated shape and stress as separate fields with adjustable correlation, where active stress was proportional to the stress director's **Q** tensor, and the active force remained linear. This is different from our approach, which incorporates nonlinear active forces and integer topological defects.

In this study, we explored the dynamics of NPC monolayers with $+1$ topological defects. Using shallow-ridged substrates to induce $+1$ topological defects (asters, spirals, and targets) within the NPC monolayers, we observed cell accumulations around defect cores and inward cellular flows toward the cores, irrespective of the defect types. Upon incorporating nonlinear active forces to linear ones, we quantitatively reproduced flow fields across all the defects. We believe that the accumulation phenomena described herein are essentially attributed to the generic properties of dense two-dimensional (2D) cellular active nematics. Chiral symmetry-breaking witnessed at various points in this study (Fig. 2f, Fig. 3f, h, Fig. 4h, Supplementary Fig. 2c) warrants further investigation as it may be related to edge flow, shear flow, and cell sorting[30,39–41].

As explained earlier, since integer defects tend to split into two $+\frac{1}{2}$ defects in nematic systems, external topographic guidance helps control experiments and reveal nonlinear active forces. Although micropatterns may seem artificial, similar situations also occur in vivo. It is known that integer defects (radial and circumferential alignment) in cell systems occur due to fiber networks (e.g., collagen) that guide cells organization[42], as shown in[20,43,44]. Therefore, studying cell interactions with external topographic features provides valuable insights into biological systems.

Our research bridges the gap in understanding the collective motion and the role of integer topological defects in 2D nematic cell layers. Defects of $+1$ topological charge provide aggregation sites, potentially affecting the cell transport and morphogenesis in vivo[45]. Furthermore, the identification of emerging nonlinear active forces will clarify our understanding of collective motion in various types of active nematics, such as those observed in bacterial colonies, cytoskeletal filaments, colloids, and three-dimensional morphogenesis[21,23,46–49]. We believe our study provides insights into the control of structure formation, highlights the effect of integer topological defects in biology, and present a new way to quantify and classify cell monolayers.

Methods

Cell culture

The cell lines of NPCs were established from mice of the standard strain E14 ICR[15] and originally from Ryoichiro Kageyama's lab. The mutants stably expressing H2B-mCherry were made by Kyogo Kawaguchi. We used Dulbecco's Modified Eagle Medium/Nutrient Mixture F-12 (DMEM/F-12) (Thermo Fisher, 11039021) as a medium base supplemented with basic fibroblast growth factor (20 ng/mL, Wako, 060-04543), epidermal growth factor (20 ng/mL, Thermo Fisher, 53003-018), and N-2 Max (100x, *R&D* Systems, AR009). 35-mm dishes were precoated with 10x diluted Matrigel (Corning, 356231) and medium (finally 30 μL Matrigel in 1 mL of the medium) overnight in 37 °C. We then removed the coating agent and uniformly placed NPCs in 2 mL of the medium. The initial cell density was approximately $5.5 * 10^{-4}/\mu m^2$. The cultures were incubated at 37 °C with 5% CO_2 at saturated humidity. StemPro Accutase (Gibco, A1110501) was used to dissociate cells during passage progress, and Stem-Cellbanker (ZENOAQ, 11922) was employed for making frozen stocks.

PDMS substrate preparation

We designed patterns in AutoCAD and accordingly produced a chromium mask, followed by lithography. Via the spin-coating of SU-8 2002 (MicroChem) at 3000 rpm, we made 1.2-μm slots on a silicon wafer after lithography. A PDMS liquid with a curing agent proportion of 1/8 (Dow Corning, Sylgard 184) was poured onto the silicon wafer and baked at 70°C for 3 h. After solidification, we peeled the PDMS sheet off the silicon wafer and finally obtained a PDMS substrate with ridges. Provided that the typical width of an elongated NPC is approximately 10 μm, to gently guide cells and not considerably hinder their movement, we fabricated ridges with a width of 9 μm and a height of 1.2 μm and set the distance between ridges to 30–120 μm. The micropatterns had a central, ridge-less area. To prevent the appearance of half-integer defects at the center, we chose the diameter of this ridgeless region as 160 μm, which was smaller than the correlation length (250 μm) in the unpatterned case (Supplementary Information Section 7). Multiple types of defects were integrated into a single PDMS sheet, facilitating

simultaneous comparisons between them. We made 4 types of PDMS sheets to measure data (PDMS1: contained $\theta_0 = 0$ and $\pi/2$, PDMS2: contained $\theta_0 = \pm\pi/12$ and $\pm 5\pi/12$, PDMS3: contained $\theta_0 = \pm\pi/6$ and $\pm\pi/3$, PDMS4: contained $\theta_0 = \pm\pi/4$). These four types of PDMS sheets were used in most of our measurements to have more statistics. PDMS sheets containing all θ_0 values were used in Fig. 1h, 1i to check the consistency of density evolution. Before seeding cells on the PDMS sheet, we applied plasma cleaner to enhance the surface hydrophilicity, sterilized with 75% ethanol and UV for 30 min separately, and washed with PBS and DMEM/F-12. Other than micropatterns presented in the main text, we also tested cell behavior on targets with R_{max} = 300, 600, and 900 μm, revealing that the consistent cell accumulations and tendency of inward flows remained unchanged.

Imaging

For long time-lapse experiments, NPCs were plated onto Matrigel-coated PDMS substrates in glass bottom dishes (Iwaki). NPCs were initially cultured in a CO_2 incubator for two days until reaching the desired confluent density, after which they were observed through phase contrast and fluorescent channels of a Leica DMi8 microscope. Tokaihit incubator, which can maintain temperature and humidity and CO_2 concentration, was assembled on the microscope to ensure normal cell growth during recording. Double-channel images were captured every 6 min to reduce phototoxicity. Steady integer topological defects induced by the guiding patterns could be observed over several days. Because three-dimensional mounds may form at defect cores, confocal microscopy (Nikon Ti2E microscope with Yokogawa CSU-W1 Sora spinning disk and Photometrics 95B CMOS camera) was used to analyze cell nuclei on the basal plane. In summary, these measurements confirmed a higher cell density (accumulation) at the cores, and the presence of inward cellular flow. See Supplementary Information (Section 9) for further details.

Nematic order

To characterize the local alignment of cells, we measured the orientational field from phase contrast images. Firstly, we computed the gradient of the bright field I_{ij}, where ij indicated the positions of image pixels. This brightness gradient was then smoothed using a Gaussian filter with a standard deviation of $\sigma = 21\,\mu$m. Subsequently, for each pixel, we built the structure tensor[15,50],

$$\mathbf{H}_{ij} = \begin{pmatrix} (\partial_x I_{ij})^2 & (\partial_x I_{ij})(\partial_y I_{ij}) \\ (\partial_x I_{ij})(\partial_y I_{ij}) & (\partial_y I_{ij})^2 \end{pmatrix} = \begin{pmatrix} H_{xx} & H_{xy} \\ H_{yx} & H_{yy} \end{pmatrix}. \tag{6}$$

The local orientation θ_{ij} and coherency C_{ij} at each pixel was then determined using the formula:

$$\theta_{ij} = \frac{1}{2}\arctan\left(\frac{2H_{xy}}{H_{xx} - H_{yy}}\right). \tag{7}$$

$$C_{ij} = \frac{\sqrt{(H_{xx} - H_{yy})^2 + 4H_{xy}^2}}{H_{xx} + H_{yy}}. \tag{8}$$

In general, a coherency close to 1 means that the structure is locally 1D, a coherency close to 0 means that there is no preferred direction. The nematic tensor order parameter Q_{ij} was calculated by

$$\mathbf{Q}_{ij} = \begin{pmatrix} \langle \cos(2\theta_{ij}) \rangle & \langle \sin(2\theta_{ij}) \rangle \\ \langle \sin(2\theta_{ij}) \rangle & \langle -\cos(2\theta_{ij}) \rangle \end{pmatrix} = \begin{pmatrix} Q_{xx} & Q_{xy} \\ Q_{yx} & Q_{yy} \end{pmatrix}, \tag{9}$$

where $\langle\cdot\rangle$ represents a spatial average calculated using a 2D Gaussian filter with standard deviation $\sigma = 42\,\mu$m. Scalar order parameter S is defined by $\sqrt{Q_{xx}^2 + Q_{xy}^2}$. The local spatial average orientational field θ was obtained from $\frac{1}{2}\arctan(Q_{xy}/Q_{xx})$. For the ideal orientations, $\theta_{ij} = \phi_{ij} + \theta_0$ in Eq. (9), ideal S is then obtained by the above steps.

We also extracted orientation fields from cell nuclei in the fluorescent images. Briefly, we employed marker-controlled watershed segmentation to detect the shapes of nuclei. Then we used ellipses to fit shapes and defined the long axis as the orientation of a single cell. See Supplementary Information (Section 4) for further detail. At last, these orientations were averaged within a 42 μm wide box to derive the local spatial average orientational fields.

We also obtained orientation fields from cell membrane signal. To label membrane, we incubated cells in 100 nM MemGlow™ (Cat. MG01) solution for 10 minutes at room temperature. By applying similar structure tensor method to membrane signals for all kinds of defects, we obtained consistent orientation and order parameter results. See Supplementary Information (Section 8) for further detail.

Cell velocity measurements

To obtain the cellular velocity, cell nuclei were tracked by TrackMate[51], a ImageJ plugin, in the fluorescent images. The LoG detector and simple LAP tracking algorithm were employed. Prior to tracking, the images were stabilized using the Image Stabilizer plugin in ImageJ. For i-th trajectory $\mathbf{r}_i(t)$, instantaneous velocity $\mathbf{v}_i(t)$ was estimated as the slope determined by $\{\mathbf{r}_i(t-2), \mathbf{r}_i(t-1), \mathbf{r}_i(t), \mathbf{r}_i(t+1), \mathbf{r}_i(t+2)\}$. The net velocity field $\mathbf{v}(x, y)$ was obtained by temporally and spatially vector averaging within a 10 μm wide box, after which a 2D Gaussian filter with standard deviation $\sigma = 42\,\mu$m was applied.

To double-check the angle distributions of net velocity fields, we also measured the cellular flows by applying an optical flow algorithm on the fluorescent images. This algorithm is rooted in the Lucas-Kanade derivative of the Gaussian method[52]. Spatial average was done with a 42 μm wide box.

In the calculation of autocorrelation of the direction of instantaneous velocity, $\langle\cos[\Delta\theta_{V_0}(dt)]\rangle = \langle\cos[\theta^i_{V_0}(t+dt) - \theta^i_{V_0}(t)]\rangle$, where $\mathbf{V}_0$ denotes instantaneous velocity, θ_{V_0} is the direction of $\mathbf{V}_0$, i is the trajectory number, $t \in$ [0, duration of i th trajectory], dt is time interval ($dt \in$ [0, duration $- t$]), and $\langle\cdot\rangle$ is the ensemble average over all the trajectories (i) and time (t). $\langle\cos[\Delta\theta_{V_0}(dt)]\rangle$ over dt can be fitted with exponential $\exp(-2dt/\tau_f)$, where τ_f is the reversal time scale. In the Fig. 3c, $k = -2/\tau_f$.

Cell density

For cell density quantification, we used the sum of fluorescent images after subtracting background. The background of fluorescent signal was calculated as the average value of the lowest 0.02% of the total pixels. See Supplementary Information (Section 5) for further detail about the transformations between fluorescent intensity and cell number.

Chirality

Reference [30] provided clear evidence that NPCs exhibited clockwise chirality, and suggested chirality was lost or reversed with Jasplakinolide treatment. In the main text, we showed our system exhibited potential clockwise chirality. To further investigate the chirality, we applied 200 nM Jasplakinolide (Sigma, J4580-100UG) every 24 hours after cells were seeded. We found this chirality was reversed, and NPCs exhibited more accumulation on the clockwise spirals with larger $|\theta_0|$. See Supplementary Information (Section 10) for further detail.

Estimation of parameters

For fitting, we normalized ρ by the mean density ρ_0. Then the eq. (5) was transfromed into

$$(I - \epsilon'\rho'\mathbf{Q})\rho'\mathbf{v} = -\zeta'\nabla\cdot\rho'\mathbf{Q} + \gamma_2'\rho'\mathbf{Q}\cdot(\nabla\cdot\rho'\mathbf{Q}) + \gamma_1'(\rho'\mathbf{Q}\cdot\nabla)\cdot\rho'\mathbf{Q} - \pi_0'\nabla\rho', \tag{10}$$

where $\epsilon' = \rho_0\epsilon, \zeta' = \zeta/\gamma_0, \gamma_2' = \gamma_2\rho_0/\gamma_0, \gamma_1' = \gamma_1\rho_0/\gamma_0, \pi_0' = \pi_0/\gamma_0, \rho' = \rho/\rho_0$. For the convenience in writtng, we set $\mathbf{f}^{\text{friction}} = (I - \epsilon'\rho'\mathbf{Q})\rho'\mathbf{v}$, $\mathbf{f}^{a1} = -\nabla\cdot\rho'\mathbf{Q}$, $\mathbf{f}^{a2} = \rho'\mathbf{Q}\cdot(\nabla\cdot\rho'\mathbf{Q})$, $\mathbf{f}^{a3} = (\rho'\mathbf{Q}\cdot\nabla)\cdot\rho'\mathbf{Q}$, $\mathbf{f}^{\text{diffusion}} = -\nabla\rho'$. Then we defined parameter vector $\mathbf{P}$ and observation vector $\mathbf{V}$

$$\mathbf{P} = (\zeta', \gamma_2', \gamma_1', \pi_0')^T, \tag{11}$$

$$\mathbf{V} = (f_{x1}^{\text{friction}}, \cdots, f_{xN}^{\text{friction}}, f_{y1}^{\text{friction}}, \cdots, f_{yN}^{\text{friction}})^T, \tag{12}$$

where the subscript $i = 1, 2, ..., N$ denotes the observation at each grid point i of fields, N is the total number of the observation points, x, y denote components in cartesian coordinates. The input matrix $\mathbf{X}$ is defined by

$$\mathbf{X} = \begin{pmatrix} f_{x1}^{a1} & f_{x1}^{a2} & f_{x1}^{a3} & f_{x1}^{\text{diffusion}} \\ \vdots & \vdots & \vdots & \vdots \\ f_{xN}^{a1} & f_{xN}^{a2} & f_{xN}^{a3} & f_{xN}^{\text{diffusion}} \\ f_{y1}^{a1} & f_{y1}^{a2} & f_{y1}^{a3} & f_{y1}^{\text{diffusion}} \\ \vdots & \vdots & \vdots & \vdots \\ f_{yN}^{a1} & f_{yN}^{a2} & f_{yN}^{a3} & f_{yN}^{\text{diffusion}} \end{pmatrix}. \tag{13}$$

Then eq. (9) can be written as $\mathbf{V} = \mathbf{XP}$.

Given that both sides of the equation contain unknown parameters, we considered a fixed ϵ' at first. We employed Bayesian inference method to keep the diffusion parameter π_0' positive[33,53]. This approach reformulated the equation into the problem of maximizing the posterior probability distribution function $\Pi(\mathbf{P}|\mathbf{V})$ of the parameter set for the given $\mathbf{V}$:

$$\Pi(\mathbf{P}|\mathbf{V}) = L(\mathbf{V}|\mathbf{P}) \times \pi(\mathbf{P}), \tag{14}$$

where the likelihood function $L(\mathbf{V}|\mathbf{P})$ was defined as

$$L(\mathbf{V}|\mathbf{P}) = \left(\frac{1}{\sqrt{2\pi\sigma^2}}\right)^{2N} \exp\left(-\frac{\|\mathbf{V} - \mathbf{XP}\|^2}{2\sigma^2}\right), \tag{15}$$

and the prior distribution of the parameter set $\pi(\mathbf{P})$ was defined as

$$\pi(\mathbf{P}) = \left(\frac{1}{\sqrt{2\pi\sigma_0^2}}\right)^3 \exp\left(-\frac{\mathbf{P_0}^T\mathbf{P_0}}{2\sigma_0^2}\right) \times \left(\frac{1}{\sqrt{2\pi\sigma_{\pi_0}^2}}\right) \exp\left(-\frac{(\pi_0' - \overline{\pi}_0)^2}{2\sigma_{\pi_0}^2}\right), \tag{16}$$

where the parameter vector was separated into two parts, $\mathbf{P_0} = (\zeta', \gamma_2', \gamma_1')^T$ and π_0'. Here, we set a positive bias ($\overline{\pi}_0 > 0$) to π_0' and assumed a Gaussian prior distribution. By maximizing the likelihood function, the optimal parameter set was obtained as

$$\mathbf{P} = (\mathbf{X}^T\mathbf{X} + \Lambda I + (\Lambda_{\pi_0} - \Lambda)I')^{-1}(\mathbf{X}^T\mathbf{V} + \Lambda_{\pi_0}\overline{\pi}_0 J), \tag{17}$$

where $\Lambda = \sigma^2/\sigma_0^2$, $\Lambda_{\pi_0} = \sigma^2/\sigma_{\pi_0}^2$, I is the identity matrix, I' is a matrix in which only element $I'(4,4) = 1$ and all other elements are 0, $J = (0, 0, 0, 1)^T$. $\overline{\pi}_0$ was set by the estimation of the diffusion constant: $\overline{\pi}_0 = v_0^2/\alpha$ where the instantaneous velocity $v_0 = 0.0067\,\mu$m/s and velocity reversal rate $\alpha = 1/3600\ \text{s}^{-1}$. The initial values of $\sigma^2, \sigma_0^2, \sigma_{\pi_0}^2$ were set as $\sigma^2 = 10^{-6}\,\mu\text{m}^2/\text{s}^2$, $\sigma_0^2 = 10^{-4}\,\mu\text{m}^4/\text{s}^2$, $\sigma_{\pi_0}^2 = 10^{-4}\,\mu\text{m}^4/\text{s}^2$. Using the calculated $\mathbf{P}$, σ^2 and σ_0^2 were updated by:

$$\sigma^2 = \frac{\|\mathbf{V} - \mathbf{XP}\|^2}{2N}, \tag{18}$$

$$\sigma_0^2 = \frac{\mathbf{P_0}^T\mathbf{P_0}}{3}, \tag{19}$$

which were subsequently used to update $\mathbf{P}$. This cycle was iterated until the relative change of the Λ per iteration became smaller than 10^{-3}.

So far, with a fixed ϵ', we obtained the estimated parameters. Next, we varied ϵ', and for each ϵ', we used the Bayesian method to obtain the estimated velocities as stated earlier. Then we calculated the determination coefficients between the estimated velocities and the measured velocities. We selected the optimal ϵ' and other parameters which maximized the determination coefficients until the relative change of determination coefficients became smaller than 10^{-5}.

Correction for the predicted outward flows of the centers

Slight outward flows appear at cores of defects with large $|\theta_0|$, where the densities are much higher (Fig. 4g, Supplementary Fig. 8a, b). Here, we neglect the $\nabla\rho$ term in eq. (5) around cores ($r < R_{min}$) according to an assumption that cells can readily move to the third dimension and form cell mounds at high density under compression. Additionally, according to Eq. (3), (4), active forces near centers are sensitive to the amplitude and gradient of S which we could not reliably measure due to equipment limitations. By using ideal orientations ($\theta = \theta_p$) and ideal S (Supplementary Fig. 9b) according to the definition of defects and setting $\pi_0' = 0$ at regions with $r < 80\,\mu$m (with other parameters as best-fit values), the outward cellular flows vanish basically (Supplementary Fig. 9a,c). This method causes fluctuations in net velocity amplitudes around $r = 80\,\mu$m (Supplementary Fig. 9a,c). To address this, we employ linear interpolation to replace the fluctuating values (Supplementary Fig. 9e).

Statistics and reproducibility

All the reported experimental results repeated successfully and independently 3 times in different weeks. Quantification always considered measurements from multiple micropatterns (N, indicated in the figure captions). Average vector fields (velocity and orientation), density fields as well as the corresponding radial profiles were obtained by averaging > 15 cellular disks for each kind of defect.

Reporting summary

Further information on research design is available in the Nature Portfolio Reporting Summary linked to this article.

Data availability

All data supporting this study and its findings are available within the article and its Supplementary Information. Any data deemed relevant are available from the corresponding author upon request. The data generated in this study are provided in the Source Data file. Source data are provided with this paper.

Code availability

The MATLAB code used for obtaining coefficients by fitting is available in Zenodo[54].

References

1. Kemkemer, R., Teichgräber, V., Schrank-Kaufmann, S., Kaufmann, D. & Gruler, H. Nematic order-disorder state transition in a liquid crystal analogue formed by oriented and migrating amoeboid cells. *Eur. Phys. J. E* **3**, 101–110 (2000).
2. Shankar, S., Souslov, A., Bowick, M. J., Marchetti, M. C. & Vitelli, V. Topological active matter. *Nat. Rev. Phys.* **4**, 380–398 (2022).
3. Notbohm, J. et al. Cellular contraction and polarization drive collective cellular motion. *Biophys. J.* **110**, 2729–2738 (2016).

4. Saw, T. B., Xi, W., Ladoux, B. & Lim, C. T. Biological tissues as active nematic liquid crystals. *Adv. Mater.* **30**, 1802579 (2018).
5. Blanch-Mercader, C. et al. Turbulent dynamics of epithelial cell cultures. *Phys. Rev. Lett.* **120**, 208101 (2018).
6. Keber, F. C. et al. Topology and dynamics of active nematic vesicles. *Science* **345**, 1135–1139 (2014).
7. Doostmohammadi, A., Thampi, S. P. & Yeomans, J. M. Defect-mediated morphologies in growing cell colonies. *Phys. Rev. Lett.* **117**, 048102 (2016).
8. Duclos, G., Erlenkämper, C., Joanny, J.-F. & Silberzan, P. Topological defects in confined populations of spindle-shaped cells. *Nat. Phys.* **13**, 58–62 (2016).
9. Sanchez, T., Chen, D. T., DeCamp, S. J., Heymann, M. & Dogic, Z. Spontaneous motion in hierarchically assembled active matter. *Nature* **491**, 431–4 (2012).
10. Balasubramaniam, L. et al. Investigating the nature of active forces in tissues reveals how contractile cells can form extensile monolayers. *Nat. Mater.* **20**, 1156–1166 (2021).
11. Copenhagen, K., Alert, R., Wingreen, N. S. & Shaevitz, J. W. Topological defects promote layer formation in myxococcus xanthus colonies. *Nat. Phys.* **17**, 211–215 (2020).
12. Giomi, L., Bowick, M. J., Ma, X. & Marchetti, M. C. Defect annihilation and proliferation in active nematics. *Phys. Rev. Lett.* **110**, 228101 (2013).
13. Lavrentovich, T. T. et al. Topology control of human fibroblast cells monolayer by liquid crystal elastomer. *Sci. Adv.* **6**, eaaz6485 (2020).
14. De Gennes, P.-G. & Prost, J.*The Physics of Liquid Crystals* (Oxford university press, 1993).
15. Kawaguchi, K., Kageyama, R. & Sano, M. Topological defects control collective dynamics in neural progenitor cell cultures. *Nature* **545**, 327–331 (2017).
16. Saw, T. B. et al. Topological defects in epithelia govern cell death and extrusion. *Nature* **544**, 212–216 (2017).
17. Vafa, F., Bowick, M. J., Shraiman, B. I. & Marchetti, M. C. Fluctuations can induce local nematic order and extensile stress in monolayers of motile cells. *Soft Matter* **17**, 3068–3073 (2021).
18. Killeen, A., Bertrand, T. & Lee, C. F. Polar fluctuations lead to extensile nematic behavior in confluent tissues. *Phys. Rev. Lett.* **128**, 78001 (2022).
19. Ma, W. et al. Cell-extracellular matrix interactions regulate neural differentiation of human embryonic stem cells. *BMC Dev. Biol.* **8**, 1–13 (2008).
20. Gogola, A., Jan, N.-J., Lathrop, K. L. & Sigal, I. A. Radial and circumferential collagen fibers are a feature of the peripapillary sclera of human, monkey, pig, cow, goat, and sheep. *Investig. Ophthalmol. Vis. Sci.* **59**, 4763–4774 (2018).
21. Hamant, O. et al. Developmental patterning by mechanical signals in arabidopsis. *Science* **322**, 1650–1655 (2008).
22. Provenzano, P. P. et al. Collagen reorganization at the tumor-stromal interface facilitates local invasion. *BMC Med.* **4**, 1–15 (2006).
23. Maroudas-Sacks, Y. et al. Topological defects in the nematic order of actin fibres as organization centres of hydra morphogenesis. *Nat. Phys.* **17**, 251–259 (2020).
24. Guillamat, P., Blanch-Mercader, C., Pernollet, G., Kruse, K. & Roux, A. Integer topological defects organize stresses driving tissue morphogenesis. *Nat. Mater.* **21**, 588–597 (2022).
25. Endresen, K. D., Kim, M., Pittman, M., Chen, Y. & Serra, F. Topological defects of integer charge in cell monolayers. *Soft Matter* **17**, 5878–5887 (2021).
26. Kaiyrbekov, K. et al. Migration and division in cell monolayers on substrates with topological defects. *Proc. Natl Acad. Sci.* **120**, e2301197120 (2023).
27. Blanch-Mercader, C., Guillamat, P., Roux, A. & Kruse, K. Integer topological defects of cell monolayers: Mechanics and flows. *Phys. Rev. E* **103**, 012405 (2021).
28. Zhao, Z. et al. Integer topological defects reveal anti-symmetric force in active nematics. *Phys. Rev. Lett.* **133**, 268301 (2024).
29. Selinger, J. V.*Introduction to the Theory of Soft Matter: From Ideal Gases to Liquid Crystals* (Springer, 2016).
30. Yamauchi, L., Hayata, T., Uwamichi, M., Ozawa, T. & Kawaguchi, K. Chirality-driven edge flow and non-Hermitian topology in active nematic cells. Preprint at https://arxiv.org/abs/2008.10852 (2020).
31. Ramaswamy, S. Active matter. *J. Stat. Mech.: Theory Exp.* **2017**, 054002 (2017).
32. Toner, J., Tu, Y. & Ramaswamy, S. Hydrodynamics and phases of flocks. *Ann. Phys.* **318**, 170–244 (2005).
33. Uwamichi, M. et al. Experimental identification of force, velocity, and nematic order relationships in active nematic cell monolayers. Preprint at https://arxiv.org/abs/2402.16151 (2024).
34. Patelli, A., Djafer-Cherif, I., Aranson, I. S., Bertin, E. & Chaté, H. Understanding dense active nematics from microscopic models. *Phys. Rev. Lett.* **123**, 258001 (2019).
35. Bertin, E. et al. Mesoscopic theory for fluctuating active nematics. *N. J. Phys.* **15**, 085032 (2013).
36. Peshkov, A., Bertin, E., Ginelli, F. & Chaté, H. Boltzmann-ginzburg-landau approach for continuous descriptions of generic vicsek-like models. *Eur. Phys. J. Spec. Top.* **223**, 1315–1344 (2014).
37. Maitra, A. et al. A nonequilibrium force can stabilize 2d active nematics. *Proc. Natl Acad. Sci.* **115**, 6934–6939 (2018).
38. Nejad, M. R. et al. Stress-shape misalignment in confluent cell layers. *Nat. Commun.* **15**, 3628 (2024).
39. Mijalkov, M. & Volpe, G. Sorting of chiral microswimmers. *Soft Matter* **9**, 6376–6381 (2013).
40. Yashunsky, V. et al. Chiral edge current in nematic cell monolayers. *Phys. Rev. X* **12**, 041017 (2022).
41. Duclos, G. et al. Spontaneous shear flow in confined cellular nematics. *Nat. Phys.* **14**, 728–732 (2018).
42. Sapudom, J. et al. Collagen fibril orientation instructs fibroblast differentiation via cell contractility. *Adv. Sci.* **10**, 2301353 (2023).
43. Hua, Y. et al. Role of radially aligned scleral collagen fibers in optic nerve head biomechanics. *Exp. Eye Res.* **199**, 108188 (2020).
44. Doyle, A. D., Nazari, S. S. & Yamada, K. M. Cell–extracellular matrix dynamics. *Phys. Biol.* **19**, 021002 (2022).
45. Alvarez-Buylla, C. L., García-Verdugo, J.-M. & Arturo. Chain migration of neuronal precursors. *Science* **271**, 978–981 (1996).
46. Basaran, M., Yaman, Y. I., Yuce, T. C., Vetter, R. & Kocabas, A. Large-scale orientational order in bacterial colonies during inward growth. *Elife* **11**, e72187 (2022).
47. Zhang, R. et al. Spatiotemporal control of liquid crystal structure and dynamics through activity patterning. *Nat. Mater.* **20**, 875–882 (2021).
48. Schaller, V., Weber, C., Semmrich, C., Frey, E. & Bausch, A. R. Polar patterns of driven filaments. *Nature* **467**, 73–77 (2010).
49. Liu, Z. T. et al. Activity waves and freestanding vortices in populations of subcritical quincke rollers. *Proc. Natl Acad. Sci.* **118**, e2104724118 (2021).
50. Jähne, B. *Spatio-temporal Image Processing: Theory and Scientific Applications* (Springer, 1993).
51. Tinevez, J.-Y. et al. Trackmate: An open and extensible platform for single-particle tracking. *Methods* **115**, 80–90 (2017).
52. Lucas, B. D. & Kanade, T. Hayes, P. J. (ed.) *An iterative image registration technique with an application to stereo vision*. (ed. Hayes, P. J.) *IJCAI'81: 7th international joint conference on Artificial intelligence*, Vol. 2, 674–679 (William Kaufmann, Vancouver, Canada, 1981).
53. Ishihara, S. & Sugimura, K. Bayesian inference of force dynamics during morphogenesis. *J. Theor. Biol.* **313**, 201–211 (2012).
54. Zhao, Z. & Sano, M. Integer topological defects offer a methodology to quantify and classify active cell monolayers. *Zenodo* https://doi.org/10.5281/zenodo.14916704 (2025).

Acknowledgements
We are grateful to Hugues Chatë, Carles Blanch-Mercader, Eric Bertin, Benoi^t Mahault, Aurelio Patelli, Jacques Prost, Sriram Ramaswamy, and Xiaqing Shi for insightful discussions. We thank Kirsten D. Endresen for making micropatterns at the initial stage. M.S. acknowledges support from the Research Fund for International Scientists of NFSC (12174254,12250710131). H.Z. acknowledges support from NSFC (12225410 and 12074243).

Author contributions
M.S., F.S., H.Z., and Z.Z. conceived and designed the research. Z.Z., H.L., and Y.Y. performed the experiments. Z.Z. analyzed the experimental data. K.K. provided materials and tools. M.S. and Y.Z. developed the theoretical part. All the authors participated in writing and revising the manuscript.

Competing interests
The authors declare no competing interests.

Additional information
Supplementary information The online version contains supplementary material available at https://doi.org/10.1038/s41467-025-57783-w.

Correspondence and requests for materials should be addressed to Masaki Sano.

Peer review information : *Nature Communications* thanks the anonymous reviewers for their contribution to the peer review of this work. A peer review file is available.